SCIENTIFIC REPORTS

OPEN

Chemical Changes in Layered Ferroelectric Semiconductors Induced by Helium Ion Beam

Received: 27 February 2017
Accepted: 20 November 2017
Published online: 30 November 2017

Alex Belianinov[1,2], Matthew J. Burch[1,2], Holland E. Hysmith[2], Anton V. Ievlev[1,2], Vighter Iberi[2,3], Michael A. Susner[4], Michael A. McGuire[4], Peter Maksymovych[1,2], Marius Chyasnavichyus[1,2], Stephen Jesse[1,2] & Olga S. Ovchinnikova[1,2]

Multi-material systems interfaced with 2D materials, or entirely new 3D heterostructures can lead to the next generation multi-functional device architectures. Physical and chemical control at the nanoscale is also necessary tailor these materials as functional structures approach physical limit. 2D transition metal thiophosphates (TPS), with a general formulae $Cu_{1-x}In_{1+x/3}P_2S_6$, have shown ferroelectric polarization behavior with a T_c above the room temperature, making them attractive candidates for designing both: chemical and physical properties. Our previous studies have demonstrated that ferroic order persists on the surface, and that spinoidal decomposition of ferroelectric and paraelectric phases occurs in non-stoichiometric Cu/In ratio formulations. Here, we discuss the chemical changes induced by helium ion irradiation. We explore the TPS compound library with varying Cu/In ratio, using Helium Ion Microscopy, Atomic Force Microscopy (AFM), and Time of Flight-Secondary Ion Mass Spectrometry (ToF-SIMS). We correlate physical nano- and micro- structures to the helium ion dose, as well as chemical signatures of copper, oxygen and sulfur. Our ToF-SIMS results show that He ion irradiation leads to oxygen penetration into the irradiated areas, and diffuses along the Cu-rich domains to the extent of the stopping distance of the helium ions.

Advances in nanofabrication are the driving force behind technological breakthroughs in performance and miniaturization. Layered materials, in particular, are beginning to take center stage as the next generation components for information technology devices[1–3]. In particular, functional layered materials with dielectric properties, such as insulators, semiconductors, and correlated electron materials will be necessary for fabrication and delivery of this new age technology[4–7].

Resist-based lithography is currently the mainstay of nanostructure fabrication, however, resist free nanofabrication directly on the surface is bringing electron, ion, and probe technologies to the forefront[8–10]. Helium Ion Microscope (HIM)[11,12], is a particularly attractive tool for nano-patterning of 2D materials *in-situ*, and is being explored by a growing number of groups world-wide[13–18]. Helium (and Neon) ion beam nanofabrication has the benefits of resist-free processing; shorter penetration depth into the bulk, and reduced parasitic ion implantation – a common issue in gallium based Focused Ion Beam (FIB) applications[11,19]. The use of a helium ion microscope (HIM) has already been demonstrated for graphene, $MoSe_2$, WSe_2 and MoS_2, through controlled ion dose exposure, and tuning of the local defect chemistry; changing the properties of these materials[15,16,20–22].

We demonstrate HIM to create a variety of micro-sized structures with varying chemical properties atop several transition metal thiophosphates (TPS); a broad class of van-der-Waals layered solids[10,13,23]. TPS exhibit strong ionic character in the chemical bonds between transition metals and the P_2S_6 framework[24]. Furthermore, these compounds have large band-gaps and a pronounced flexibility in ionic substitution of the metal sites; with over 260 combinations known for the sulfides alone. Some of these compounds support coherent ordering of metal ions across layers, with ferroelectric and anitferroelectric ground states[14,15], dielectric relaxor behavior[16,17], and associated phase transitions. A combination of experimental techniques revealed that the $Cu_{1-x}In_{1+x/3}P_2S_6$ system undergoes chemical phase separation into centrosymmetric $In_{4/3}P_2S_6$ and ferroelectric $CuInP_2S_6$ while

[1]The Institute for Functional Imaging of Materials, Oak Ridge National Laboratory, Oak Ridge, TN, 37831, USA. [2]Center for Nanophase Materials Sciences, Oak Ridge National Laboratory, Oak Ridge, TN, 37831, USA. [3]Department of Materials Science and Engineering, University of Tennessee, Knoxville, Knoxville, TN, 37996, USA. [4]Materials Sciences and Technology Division, Oak Ridge National Laboratory, Oak Ridge, TN, 37831, USA. Correspondence and requests for materials should be addressed to O.S.O. (email: ovchinnikovo@ornl.gov)

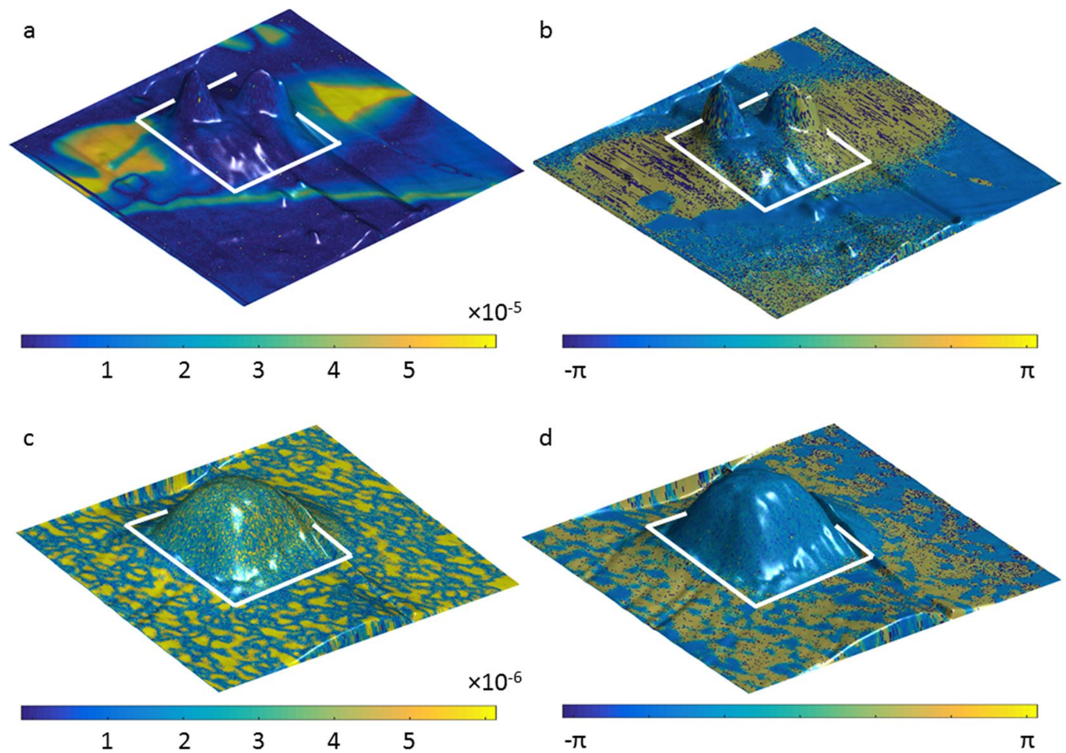

Figure 1. Band Excitation Piezoresponse Force Microscopy (BE-PFM) results. The BE-PFM signal color map, for all figures, is overlaid on the AFM topography. White boxes, in all panels, indicate the HIM irradiated areas. (**a**) The BE-PFM amplitude of the $Cu_{0.19}$ sample; (**b**) The BE-PFM phase of the $Cu_{0.19}$ sample; (**c**) The BE-PFM amplitude of the $Cu_{0.70}$ sample; (**d**) The BE-PFM phase of the $Cu_{0.70}$ sample.

maintaining layered framework of the parent compound. The structural coherence of the decomposition enables the increase of the ferroelectric T_c to 335 K, making Cu-deficient $Cu_{1-x}In_{1+x/3}P_2S_6$ the highest temperature layered, van-der-Waals gapped ferroelectric material yet known[25].

Our earlier work demonstrates that by controlling the helium dose on a $CuInP_2S_6$ with a 1:1 stoichiometric ratio of Cu/In yields a loss in ferroelectricity, and growth of conical structures that scale in volume with the ion dose[18,26]. However, the nature of the growth process and the exact chemical composition of the ensuing nanostructures remained a mystery. In this work, we explore the helium ion surface interaction within a library of the TPS materials, $Cu_{1-x}In_{1+x/3}P_2S_6$, with the adjusted Cu ratios ranging from 5 to 100% in order to elucidate their chemical structure. We use Atomic Force Microscopy (AFM), to check the veracity of micro- and nano- sized structures, as well as Secondary Ion Mass Spectrometry (SIMS) to track the chemical changes in the helium irradiated area. Our results demonstrate that copper concentration dictates the sizes of the nanostructures, as the same helium dose applied to the same area yields different volumes in the final protrusions.

Results

Throughout the article we will use the values for the Cu concentration only, in order to represent different compound formulae, *i.e*. $Cu_{0.05}$ for $Cu_{0.05}In_{1.32}P_2S_6$. Large, defect-free terraces on TPS were prepared using standard graphene exfoliation techniques. The TPS samples were mounted on conductive carbon tape (PELCO Tabs™, Ted Pella 16084-3) and grounded via stainless steel pucks in AFM and HIM experiments (see Methods section for details). To investigate the effects of the stoichiometric ratio of Cu/In on the growth of the nanostructures, we irradiated the samples with different Cu compositions with an array of He doses. Figure 1(a–d) shows Band Excitation Piezoresponse Force Microscopy[27] (BE-PFM) amplitude (a, c) and phase (b, d) signals overlaid on the 3D surface topography; the irradiated regions for the $Cu_{0.19}$ Fig. 1(a,b) and $Cu_{0.70}$ Fig. 1(c,d) are highlighted by white boxes. Pure topography images can be found in Suppl. Mat. Fig. S5. Ferroelectric domain networks of the Cu rich phase are shown in yellow in Fig. 1(a,b) for $Cu_{0.19}$ and Fig. 1(c,d) for $Cu_{0.70}$ respectively. Note the sharp domain discontinuity in the $Cu_{0.19}$ samples visible in both the amplitude Fig. 1a and the phase Fig. 1b signals. It is especially well resolved in the phase signal, where the ferroelectric domain (yellow region) is bisected by the ion exposure (blue region) within the white box. The ToF-SIMS results, discussed in more detail below, show that oxygen replaces sulfur ions, which results in the growth of vertical structures within the exposed area. The authors note, that the samples are exposed to atmosphere during the transfer between the HIM and the ToF-SIMS, as well as during the AFM experiments. Furthermore, our HIM mounted residual gas analyzer (Stanford Instruments, RGA 200) indicates the presence of oxygen and water at 1×10^{-8} torr and 6×10^{-8} torr respectively in the HIM chamber even after a heavy plasma clean. Therefore, oxidation may occur within the HIM chamber immediately as the TPS surface is exposed to the beam. Additionally, as can be seen from Fig. 1a, irradiated areas with the

ferroelectrically active Cu phase (yellow in panels a, c) grow wider and taller, as opposed to the paraelectric, $In_{4/3}P_2S_6$, areas shown in blue. The behavior is also similar in $Cu_{0.70}$ illustrated in Fig. 1(b,d) as a large cubic structure. Interestingly, at higher Cu concentrations the entire irradiated area as well as a small percentage of the surrounding area grow isotropically, presumably due to a more consistent Cu dispersion. Earlier ambient and vacuum BE-PFM studies have shown regions of ferroelectric $CuInP_2S_6$ and dielectric $In_{4/3}P_2S_6$ coexisting within each layer of the sample[26], where the ferroelectric phase consisted of continuous domains of oppositely oriented out-of-plane polarization. PFM carried out in this work after modification by HIM showed similar domain structure in the unperturbed areas of the sample (yellow domains in Fig. 1(c,d)).

Figure 2 illustrates the relationship between the area and the volume of modified regions as a function of He-ion dose, and sample composition. We irradiated all samples with rectangular patterns, 1 μm long and 50, 100, 250 nm wide. Unfortunately, since the domain distribution cannot be visualized directly in the HIM, we could not ensure that the nanostructure area is limited to the purely ferroelectric or the dielectric phase. This may be related to the relatively large standard deviation in all plots. On the other hand, for the purpose of creating functional nanostructures, such as interconnects and heterogeneous 2D material stacks; both dielectric and ferroelectric areas are pertinent. Figure 2(a,b) is the area and volume of the resultant structures within the rectangular are exposed to helium irradiation as measured by AFM. The general trend shows increasing area and volume as a function of dose, especially for higher copper concentration samples. Figure 2c is the full width half-max (FWHM) of averaged data for the 50, 100, and 250 nm lines written on $Cu_{0.05}$ (open symbols) and $Cu_{0.70}$ (filled symbols) with doses ranging from 2×10^{14} to 1×10^{15} ions/cm^2. In both samples, the widths of the lines do not follow any observable trend with increasing dose, likely due to a mixture of the paraelectric and the ferroelectric phases in the areas of helium exposure. Furthermore, the difference in the smallest possible structures is also probably tied to interaction volume of the helium ions with the bulk material. If we assume a uniform target density of 2.8470 g/cm^3 based on stoichiometric ratios for $Cu_{0.70}$ the helium ion projected range at 30 keV is 274 nm (calculated by the IONiSE[28] simulation) which is similar in size to the patterned structures. However, in the copper poor samples such as the $Cu_{0.05}$, the density and penetration depth can vary greatly locally. Therefore, a potential pathway to reduce structure size would be to limit the helium ion interaction with the material by irradiating individual 2D flakes of only a few layers, where the structure size would nominally be determined by the flake thickness.

To investigate the chemical composition of the nanostructures we carried out time of flight secondary ion mass spectrometry (ToF-SIMS) measurements, with an IONTOF SIMS.5 instrument using a Bismuth primary source and a Cesium sputtering source. ToF-SIMS measurements (Fig. 3, Supplementary Figs S1 and S2) have shown significant amounts of oxygen on the surface and in the bulk of irradiated regions (Fig. 3(a,c,e and g,i,k), which suggests the origin of these changes is the He-ion irradiation. Intensity signal profiles for the sulfur and oxygen signal are shown in Suppl. Mat. Figs S3 and S4. Furthermore, ToF-SIMS results show a decrease in the sulfur concentration near irradiated regions, seen as a halo in the S^- signal, Fig. 3(b,d,f and h,j,l). Detailed analysis of the ToF-SIMS data revealed a significant difference in the oxidation levels of the samples with different compositions. Sample with lower Cu concentration ($Cu_{0.05}$; Fig. 3(a–f)) show deeper penetration of oxygen into the irradiated squares (Fig. 3(a,c,e)). While in the samples with higher Cu concentration, ($Cu_{0.70}$ Fig. 3(g–l)) the depth of the oxygen penetration was much smaller (Fig. 3g,i,k). Although, ToF-SIMS measurements allow bulk measurements, we were not able to quantitatively measure the depth of ToF-SIMS imaging, as the sputtering rates in these complex multicomponent samples are difficult to estimate. However, since the density of both samples is relatively close, we can qualitatively compare the depth of oxygen penetration. In the $Cu_{0.05}$ samples, oxygen levels were elevated after 1500 seconds of sputtering. Whereas in the $Cu_{0.70}$ samples, oxygen disappeared after about 400 seconds of sputtering. Interestingly, the $Cu_{0.70}$ sample showed significant lateral oxidation outside of the irradiated regions. This hints at the kinetics of the oxidation process, which are likely to be two-step with a (i) quick lattice destruction, followed by (ii) slower oxygen diffusion. SIMS imaging beyond the surface layer, shows oxygen inside irradiated squares only, (Fig. 3f) however, these SIMS images are taken after 400 s of Cs gun sputtering, penetrating well within the sample bulk, and illustrate oxygen signal spreading laterally outside the irradiated region (Fig. 3e,k). The observed oxygen depth penetration difference between the two compositions could also be responsible for the difference in the structure size observed in Fig. 2 since oxidation seems to be the dominant chemical change after the irradiation process.

Discussion

In summary, we have explored the effect of helium ion irradiation on the surfaces of a library of TPS compounds using AFM and ToF-SIMS. After the helium exposure, we have used the AFM to observe surface nano- and micro- structures that scale in area and volume, to the total dose of the helium ion beam, as well as the overall copper concentration in the sample. Furthermore, our ToF-SIMS results show that after ion irradiation, the oxygen concentration in the irradiated areas is significantly increased. In samples with lower Cu concentration the oxygen penetration was higher than in samples with more copper. Finally, nanostructured patterns, consisting of lines 50, 100, and 250 nm wide and 1 μm long, atop the library of TPS compounds with varying copper concentrations, reveal a general trend on decreasing structure veracity as the copper concentration is increased.

Methods

Sample Synthesis. TPS crystals were grown by chemical vapor transport in evacuated quartz ampoules. The In_2S_3 precursor was prepared from Indium (Alfa Aesar Puratronic 99.999%) and Sulphur (JMC Puratronic 99.999%) by reacting them in an appropriate stoichiometric mixture at 950 °C for 48 hrs. In_2S_3 product was ground into powder, and checked for purity by using X-ray diffraction. We then added the necessary quantities of Cu, P, and S (Alfa Aesar, Puratronic 99.999%+) to obtain the compositions tested. We combined these precursors in a mortar and pestle in a He-filled glovebox, loaded the powder into quartz ampoules, and sealed under vacuum. The ampoules were brought to 750–775 °C over a period of 15 hrs in a box furnace, held at temperature for

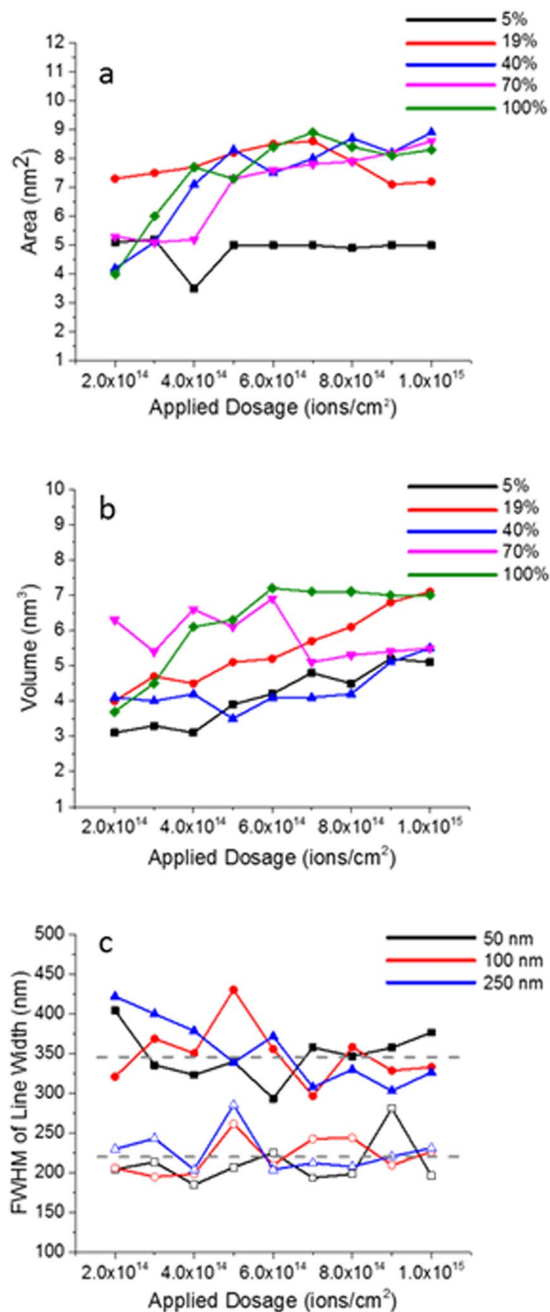

Figure 2. Statistics of the exposed regions on TPS compound library. (**a**) Area of the resulting structures for $1 \times 1\,um^2$ exposed areas as a function of dose. Different color lines represent different copper concentrations supplemented by a legend in the upper right. (**b**) Volume of the resulting structures for $1 \times 1\,um^2$ exposed areas as a function of dose. Different color lines represent different copper concentrations supplemented by a legend in the upper right. (**c**) Full Width Half Max (FWHM) of the irradiated lines 1 um long with varying widths as shown by different color lines supplemented by the legend in the upper right. Two sets of samples are presented the low and the high copper concentration the $Cu_{0.05}$ (open symbols) and the $Cu_{0.7}$ (solid symbols).

96 hrs., and then cooled at a rate of 20 °C/hr. to 30 °C. After cooling, the crystals were extracted by slicing open the ampoules. The products appear as platelets ranging in area from 2 to 1 mm² and approximately <150 μm thick. TPS samples were mounted on to metal disks (Ted Pella Prod. No. 16218) with a conductive carbon tape; with a grounding wire attached directly to the disk. A clean surface was prepared by "Scotch tape method" widely used for graphene preparation[29].

Ambient Imaging. Ambient Band Excitation Imaging was done on a Cypher AFM ES manufactured Asylum Research. Pt-Cr coated Multi-75EG AFM cantilevers (purchased from NanoAndMore) have been used for imaging all samples. For contact mode PFM and topography measurements a setpoint of 0.75–1 V was used.

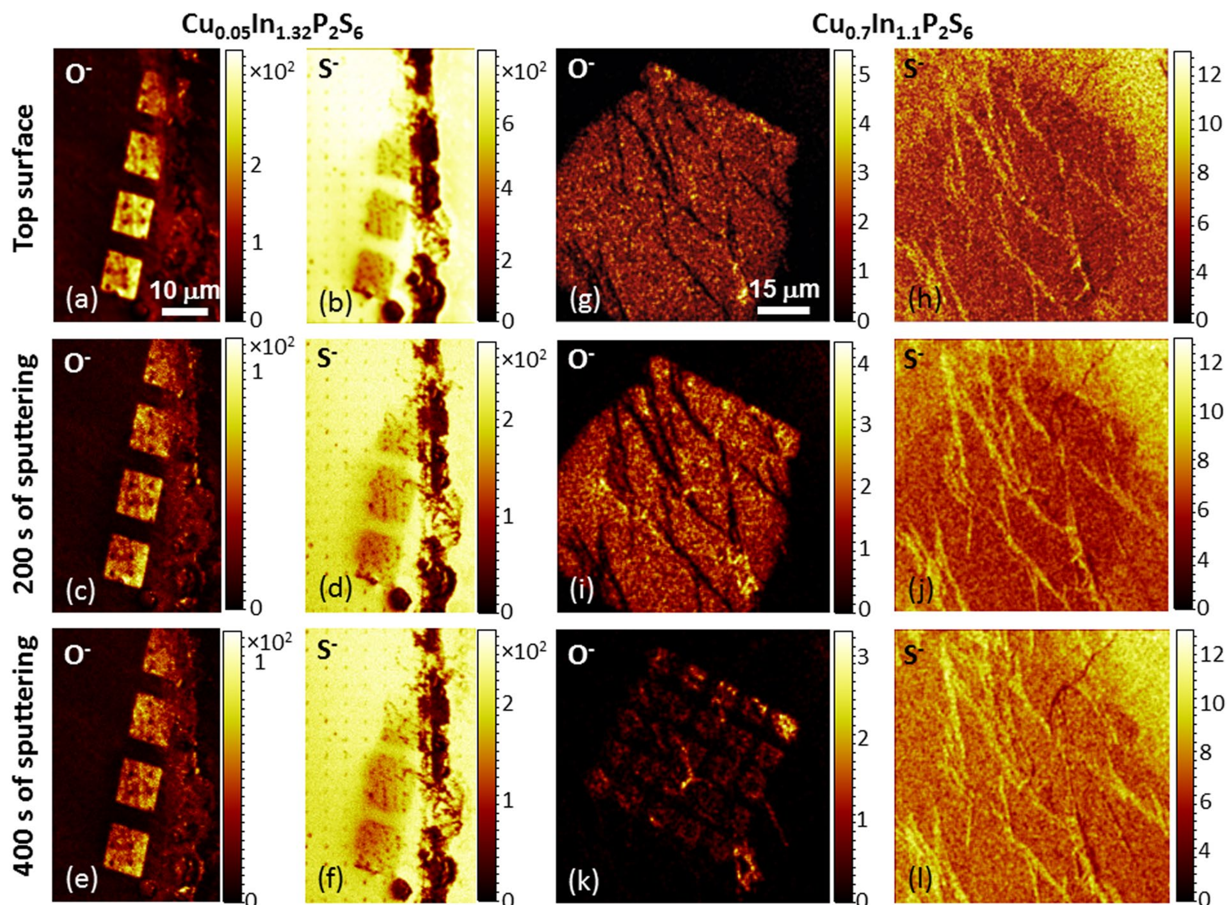

Figure 3. Time of Flight Secondary Ion Mass Spectrometry (ToF-SIMS) results on irradiated helium ion irradiated regions for $Cu_{0.05}In_{1.32}P_2S_6$ (panels a–f) & $Cu_{0.7}In_{1.1}P_2S_6$ (panels g–l) (**a**) O^- signal for $Cu_{0.05}In_{1.32}P_2S_6$ at the surface of the sample with no Cs sputtering; total ion count 1.97×10^6 (**b**) S^- signal for $Cu_{0.05}In_{1.32}P_2S_6$ at the surface of the sample with no Cs sputtering; total ion count 2.52×10^7 (**c**) O^- signal for $Cu_{0.05}In_{1.32}P_2S_6$ at the surface of the sample after 200 s of Cs sputtering; total ion count 6.72×10^5 (**d**) S^- signal for $Cu_{0.05}In_{1.32}P_2S_6$ at the surface of the sample after 200 s of Cs sputtering; total ion count 7.71×10^6 (**e**) O^- signal for $Cu_{0.05}In_{1.32}P_2S_6$ at the surface of the sample after 400 s of Cs sputtering; total ion count 6.45×10^6 (**f**) S^- signal for $Cu_{0.05}In_{1.32}P_2S_6$ at the surface of the sample after 400 s of Cs sputtering; total ion count 7.63×10^6 (**g**) O^- signal for $Cu_{0.7}In_{1.1}P_2S_6$ at the surface of the sample with no Cs sputtering; total ion count 5.92×10^4 (**h**) S^- signal for $Cu_{0.7}In_{1.1}P_2S_6$ at the surface of the sample with no Cs sputtering; total ion count 4.40×10^5 (**i**) O^- signal for $Cu_{0.7}In_{1.1}P_2S_6$ at the surface of the sample after 200 s of Cs sputtering; total ion count 5.23×10^4 (**j**) S^- signal for $Cu_{0.7}In_{1.1}P_2S_6$ at the surface of the sample after 200 s of Cs sputtering; total ion count 4.96×10^5 (**k**) O^- signal for $Cu_{0.7}In_{1.1}P_2S_6$ at the surface of the sample after 400 s of Cs sputtering; total ion count 1.15×10^4 (**l**) S^- signal for $Cu_{0.7}In_{1.1}P_2S_6$ at the surface of the sample after 400 s of Cs sputtering; total ion count 5.32×10^5.

All Band Excitation images were collected at frequency ranges around the third excitation mode of the cantilever (300–400 kHz), using the IgorPro control software as well as in house National Instruments based hardware and software; additional image post-processed was done in WsXM[30], and Matlab.

Helium-Ion Microscopy. Scanning helium-ion microscopy measurements were done on a Zeiss ORION Nanofab He+/Ne+ microscope, at 20 kV accelerating voltage, beam current of ~3.0 pA, and chamber base pressure of 1.5×10^{-7} mTorr. The sample was irradiated with a He+ beam with dwell time of 0.5 μs and 10 × 10 nm pixel spacing, the ion dose was varied from 1×10^{14} to 1×10^{18} ions/cm^2. To minimize ion beam damage and enable subsequent identification of the irradiated regions of interest we acquired low magnification secondary electron images of the nanostructured regions.

Time of flight Secondary Ion Mass Spectroscopy

ToF SIMS measurements were performed in positive ions detection mode using TOF SIMS-5 (ION-TOF GmbH, Germany) using a 30 keV Bi ion gun as the primary source with a focused ion beam spot size of ~120 nm, current ~500 nA and a $m/\Delta m$ resolution of 60 ÷ 200. The images were collected with a resolution of 256 × 256 points across 80 and 60 μm imaging areas. Depth profiling of the sample was carried out using a Cs^+ ion-sputtering source operated at 1 keV and 60 nA, and sputtering for 5 ÷ 10 s per slice over a 200 μm total area. The data was collected in negative ions detection mode.

References

1. Chhowalla, M. *et al*. The chemistry of two-dimensional layered transition metal dichalcogenide nanosheets. *Nature chemistry* **5**, 263–275 (2013).
2. Tongay, S. *et al*. Defects activated photoluminescence in two-dimensional semiconductors: interplay between bound, charged, and free excitons. *Scientific reports* **3** (2013).
3. Jariwala, D., Sangwan, V. K., Lauhon, L. J., Marks, T. J. & Hersam, M. C. Emerging device applications for semiconducting two-dimensional transition metal dichalcogenides. *ACS nano* **8**, 1102–1120 (2014).
4. Huang, Y., Liang, J. J. & Chen, Y. S. An Overview of the Applications of Graphene-Based Materials in Supercapacitors. *Small* **8**, 1805–1834, https://doi.org/10.1002/smll.201102635 (2012).
5. Osada, M. & Sasaki, T. Two-Dimensional Dielectric Nanosheets: Novel Nanoelectronics From Nanocrystal Building Blocks. *Advanced Materials* **24**, 210–228, https://doi.org/10.1002/adma.201103241 (2012).
6. Morales-Narvaez, E. & Merkoci, A. Graphene Oxide as an Optical Biosensing Platform. *Advanced Materials* **24**, 3298–3308, https://doi.org/10.1002/adma.201200373 (2012).
7. Ma, R. Z. & Sasaki, T. Nanosheets of Oxides and Hydroxides: Ultimate 2D Charge-Bearing Functional Crystallites. *Advanced Materials* **22**, 5082–5104, https://doi.org/10.1002/adma.201001722 (2010).
8. Jesse, S. *et al*. Directing Matter: Towards Atomic Scale 3D Nanofabrication. *ACS Nano*, https://doi.org/10.1021/acsnano.6b02489 (2016).
9. Stampfer, C. *et al*. Tunable Coulomb Blockade in Nanostructured Graphene. *Applied Physics Letters* **92**, 012102 (2008).
10. Schnez, S. *et al*. Observation of Excited States in a Graphene Quantum Dot. *Applied Physics Letters* **94**, 012107 (2009).
11. Joy, D. C. *Helium Ion Microscopy: Principles and Applications*. First edn, (Springer, 2013).
12. Hlawacek, G., Veligura, V., van Gastel, R. & Poelsema, B. Helium ion microscopy. *Journal of Vacuum Science & Technology B* **32**, 020801 (2014).
13. Naitou, Y., Iijima, T. & Ogawa, S. Direct Nano-Patterning of Graphene with Helium Ion Beams. *Applied Physics Letters* **106**, 033103 (2015).
14. Fox, D. S. *et al*. Nanopatterning and Electrical Tuning of MoS2 Layers with a Subnanometer Helium Ion Beam. *Nano letters* **15**, 5307–5313 (2015).
15. Iberi, V. *et al*. Maskless Lithography and *In Situ* Visualization of Conductivity of Graphene using Helium IonMicroscopy. *Scientific Reports* **5**, 11952, https://doi.org/10.1038/srep11952 (2015).
16. Stanford, M. G. *et al*. Focused helium-ion beam irradiation effects on electrical transport properties of few-layer WSe2: enabling nanoscale direct write homo-junctions. *Scientific reports* **6**, 27276 (2016).
17. Iberi, V. *et al*. Nanoforging Single Layer MoSe2 Through Defect Engineering with Focused Helium Ion Beams. *Scientific Reports* **6**, 30481 (2016).
18. Belianinov, A. *et al*. *Polarization control via He-ion beam* induced nanofabrication in layered ferroelectric semiconductors. *ACS applied materials & interfaces* **8**, 7349–7355 (2016).
19. Saad, M. M., Bowman, R. M. & Gregg, J. M. Characteristics of Single Crystal "Thin Film" Capacitor Structures Made Using a Focused Ion Beam Microscope. *Applied Physics Letters* **84**, 1159–1161, https://doi.org/10.1063/1.1645318 (2004).
20. Yoon, K. *et al*. Atomistic-Scale Simulations of Defect Formation in Graphene Under Noble Gas Ion Irradiation. *ACS Nano* (2016).
21. Fox, D., Chen, Y., Faulkner, C. C. & Zhang, H. Nano-structuring, surface and bulk modification with a focused helium ion beam. *Beilstein journal of nanotechnology* **3**, 579–585 (2012).
22. Fox, D. *et al*. Helium ion microscopy of graphene: beam damage, image quality and edge contrast. *Nanotechnology* **24**, 335702 (2013).
23. Ievlev, A. V., Susner, M. A., McGuire, M. A., Maksymovych, P. & Kalinin, S. V. Quantitative analysis of the local phase transitions induced by laser heating. *ACS nano* **9**, 12442 (2015).
24. Susner, M. A. *et al*. Cation-Eutectic Transition Via Sublattice Melting in CuInP2S6/In4/3P2Sαan der Waals Layered Crystals. *ACS nano* (2017).
25. Liu, F. *et al*. Room-temperature ferroelectricity in CuInP2S6 ultrathin flakes. *Nature Communications* **7** (2016).
26. Belianinov, A. *et al*. CuInP2S6 - Room Temperature Layered Ferroelectric. *Nano Letters* **15**, 3808–3814, https://doi.org/10.1021/acs.nanolett.5b00491 (2015).
27. Jesse, S. *et al*. Band Excitation in Scanning Probe Microscopy: Recognition and Functional Imaging. *Annual Review of Physical Chemistry* **65**, 519–536, https://doi.org/10.1146/annurev-physchem-040513-103609 (2014).
28. Ramachandra, R., Griffin, B. & Joy, D. A model of secondary electron imaging in the helium ion scanning microscope. *Ultramicroscopy* **109**, 748–757 (2009).
29. Novoselov, K. S. *et al*. Electric Field Effect in Atomically Thin Carbon Films. *Science* **306**, 666–669, https://doi.org/10.1126/science.1102896 (2004).
30. Horcas, I. *et al*. WSXM: A Software for Scanning Probe Microscopy and a Tool for Nanotechnology. *Review of Scientific Instruments* **78**, 013705, https://doi.org/10.1063/1.2432410 (2007).

Acknowledgements

Research was supported (M.B., H.H., V.I., A.V.I., M.C., P.M., O.S.O.) and partially conducted (AFM, HIM, ToF-SIMS) at the Center for Nanophase Materials Sciences, which is sponsored at Oak Ridge National Laboratory by the Scientific User Facilities Division, Office of Basic Energy Sciences, US Department of Energy. Research for HIM – A. B., crystal growth – M.A.S. and M.A.M. was partially sponsored by the Laboratory Directed Research and Development Program of Oak Ridge National Laboratory, managed by UT-Battelle, LLC, for the U. S. Department of Energy.

Author Contributions

A.B., M.J.B., O.S.O. designed the experiment, compiled the manuscript H.H. and S.J., collected the BE and AFM data. A.B., M.J.B., V.I., A.V. I. provided the HIM and SIMS expertise as well as images. M.A.S., M.A.M., P.M., M.C. conducted the sample growth and sample preparation. All authors contributed to writing and editing of the manuscript.

Additional Information

Supplementary information accompanies this paper at https://doi.org/10.1038/s41598-017-16949-3.

Competing Interests: The authors declare that they have no competing interests.

Publisher's note: Springer Nature remains neutral with regard to jurisdictional claims in published maps and institutional affiliations.

Open Access This article is licensed under a Creative Commons Attribution 4.0 International License, which permits use, sharing, adaptation, distribution and reproduction in any medium or format, as long as you give appropriate credit to the original author(s) and the source, provide a link to the Creative Commons license, and indicate if changes were made. The images or other third party material in this article are included in the article's Creative Commons license, unless indicated otherwise in a credit line to the material. If material is not included in the article's Creative Commons license and your intended use is not permitted by statutory regulation or exceeds the permitted use, you will need to obtain permission directly from the copyright holder. To view a copy of this license, visit http://creativecommons.org/licenses/by/4.0/.

© The Author(s) 2017